Millisecond dynamics of colloidal suspension studied by X-ray photon correlation spectroscopy at the Shanghai Synchrotron Radiation Facility*

Chen-Hui Cui [2,3] Zi-Mu Zhou,[3,4] Lin-Feng Wei,[5] Song-Lin Li,[2,3] Feng Tian [1] Xiu-Hong Li,[1] Zhi Guo,[1,†] Yi-Hui Xu,[5,‡] Huai-Dong Jiang [2,5] and Ren-Zhong Tai[1,2,§]

[1] *Shanghai Synchrotron Radiation Facility, Shanghai Advanced Research Institute, Chinese Academy of Sciences, Shanghai 201204, China*
[2] *School of Physical Science and Technology, ShanghaiTech University, Shanghai 201210, China*
[3] *Shanghai Institute of Applied Physics, Chinese Academy of Sciences, Shanghai 201800, China*
[4] *University of Chinese Academy of Sciences, Chinese Academy of Sciences, Beijing 100049, China*
[5] *Center for Transformative Science, ShanghaiTech University, Shanghai 201210, China*

X-ray photon correlation spectroscopy (XPCS) has emerged as a powerful tool for probing the nanoscale dynamics of soft condensed matter and strongly correlated materials owing to its high spatial resolution and penetration capabilities. This technique requires high brilliance and beam coherence, which are not directly available at modern synchrotron beamlines in China. To facilitate future XPCS experiments, we modified the optical setup of the newly commissioned BL10U1 USAXS beamline at the Shanghai Synchrotron Radiation Facility (SSRF). Subsequently, we performed XPCS measurements on silica suspensions in glycerol, which were opaque owing to their high concentrations. Images were collected using a high frame rate area detector. A comprehensive analysis was performed, yielding correlation functions and several key dynamic parameters. All the results were consistent with the theory of Brownian motion and demonstrated the feasibility of XPCS at SSRF. Finally, by carefully optimizing the setup and analyzing the algorithms, we achieved a time resolution of 2 ms, which enabled the characterization of millisecond dynamics in opaque systems.

Keywords: XPCS, SSRF, Silica suspension, Glycerol, Brownian motion, Millisecond dynamics

I. INTRODUCTION

When coherent light impinges on a disordered sample, the resulting scattered signal forms a speckle pattern. Because the internal structure of the disordered sample evolves over time, the corresponding speckle pattern also fluctuates. Valuable insights into the internal dynamics of the sample can be obtained by analyzing the correlations between these fluctuating speckle patterns. Using this principle, dynamic light scattering (DLS) techniques that utilize coherent visible light have been developed for approximately half a century, facilitating the exploration of numerous intricate dynamics and relaxation processes in condensed systems [1–5]. A fundamental assumption during the correlation of the operational scattering signals is that the photons detected by the detector are scattered only once by the sample, thereby excluding the effect of multiple scattering events. However, in the visible light spectrum, the probability of a single photon undergoing multiple scatterings becomes significant when the concentration of the sample under investigation is excessively high or the sample is optically opaque [6]. Therefore, DLS is typically utilized only for analyzing materials with low concentrations or minimal absorption.

Owing to this limitation, XPCS techniques that use (partially) coherent X-rays as a substitute for visible light have emerged, thereby enabling the examination of highly concentrated or optically opaque materials [7]. This is primarily because the scattering cross-section of X-rays is smaller than that of visible light [8]. This results in reduced susceptibility to multiple scattering during the experiment. In addition, the shorter wavelength of X-rays enables the detection of samples with smaller length scales [9]. However, the smaller scattering cross section of the X-rays also results in a weaker scattering signal. When the number of coherent photons in the (partially) coherent X-ray beam is equivalent to that in a laser, XPCS experiments become more challenging than DLS experiments, resulting in poor signal-to-noise ratio (SNR) of the data obtained. Consequently, the coherent X-ray flux is a primary limiting factor for the development of XPCS. The solution can be derived from the SNR equation [10]:

$$SNR \propto I_{\mathrm{pix}} \times (N_{\mathrm{pix}} N_{\mathrm{fr}} N_{\mathrm{rep}})^{1/2}. \quad (1)$$

where I_{pix} denotes the average intensity per pixel, which is associated with the incident coherent flux. N_{pix}, $N_t extfr$, and N_{rep} denote the number of pixels, number of frames, and number of repetitions, respectively. I_{pix} can be enhanced by designing a dedicated XPCS beamline (for instance, focusing the beam using compound refractive lenses). Likewise, the coherent X-ray flux is anticipated to increase by several orders of magnitude by adopting more advanced fourth-generation X-ray sources, such as near diffraction-limited storage rings (DLSRs) [11–16] and free-electron lasers (FELs) [17–22]. N_{pix} can be improved using area detectors along with the multi-speckle XPCS method [23]. Both N_{rep} and N_{fr} enhance the SNR by increasing the number of sampled frames.

Another limitation of the XPCS is its relatively low tem-

* This work was supported by National Natural Science Foundation of China (No. 12075304), Natural Science Foundation of Shanghai (No. 22ZR1442100) and National Key Research and Development Program of China (No. 2022YFB3503904).
† guoz@sari.ac.cn
‡ xuyh1@shanghaitech.edu.cn
§ tairz@sari.ac.cn

poral resolution that primarily arises from the lower (partially) coherent flux employed in XPCS experiments. For instance, at a constant coherent flux, increasing the detector frame rate requires a corresponding reduction in the exposure time, which in turn lowers the value of I_{pix}. According to Eq. 1, this decrease in I_{pix} reduces the SNR. Therefore, both high SNR and high temporal resolution are impossible to achieve simultaneously, as these two factors are inversely related to one another. The temporal resolution of XPCS was constrained to ensure that XPCS experimental data had a sufficiently high SNR. Furthermore, the maximum detection frame rate of the area detectors employed in XPCS experiments presented a notable constraint [7, 9]. With the development of fourth-generation X-ray sources and the introduction of higher-frame-rate detectors, the range of XPCS detection times is expected to expand, particularly for the fastest dynamics [9, 24, 25]. After more than two decades of development, XPCS has been extensively applied to condensed systems [9, 26], including colloidal suspensions [23, 27], polymers [28, 29], metallic glasses [30, 31], proteins [32–34], and strongly correlated materials [10, 35, 36].

SSRF is the first third-generation synchrotron radiation light source in China. In recent years, its experimental capability has increased [37–41]. More recently, the SSRF commissioned all its second-phase beamlines that employ state-of-the-art undulators to provide significantly higher beam quality. This endeavor will facilitate the development of coherent technology that has already achieved results in coherent diffraction imaging (CDI) and scanning coherent diffraction imaging (scanning CDI or ptychography) at the SSRF [42–44]. However, significant progress is yet to be achieved in XPCS experiments. In addition, the absence of a dedicated XPCS beamline at SSRF presents challenges for conducting XPCS experiments.

In this work, we demonstrated the feasibility of XPCS at the SSRF with millisecond time resolution by optimizing the optics, samples, and analysis algorithm. The experiments employed standard silica colloidal suspensions as samples, which were ideal for XPCS experiments owing to their relatively simple and clear dynamic mechanisms. Furthermore, colloidal particles can serve as tracer particles to reveal structural changes in the sample through their dynamic alterations, such as glass transition [45, 46] and non-equilibrium dynamics of soft materials [47]. Consequently, understanding the dynamic processes of dilute colloidal suspensions is beneficial for further investigations of related materials.

II. SAMPLE PREPARATION

An aqueous suspension of silica spheres (M814153, MACKLIN, $500\,\mathrm{nm}$) was used as the stock solution in this experiment. Characterized by scanning electron microscopy (SEM), the diameter of the silica spheres of the stock solution was determined by evaluating at least 1000 particles in the image. An average size of $R_{\mathrm{SEM}} = 524.4\,\mathrm{nm}$ and dispersion of $p = 7.2\ \%$ were obtained [27]. The volume fraction of silica in the stock solution was 1%. But the diffusion of silica in water was too rapid for the Eiger X 4M detector in the range of the observable. To better characterize the dynamics, the stock solution was mixed with glycerol at a volume ratio of $1:1$. Most of the water was removed using a rotary evaporator, yielding considerably slower diffusion [45, 48]. The actual volume fraction of silica was slightly lower than 1% because the rotary evaporator could not completely remove the residual water. The interactions between silica particles can be neglected at this volume fraction [46]. Before the XPCS experiment, the suspension was sonicated and injected into a $2\,\mathrm{mm}$-thick sample cell, which was sealed with Kapton film. The experiment was conducted at a temperature of approximately $\sim 298\,\mathrm{K}$.

III. EXPERIMENTAL CONFIGURATION

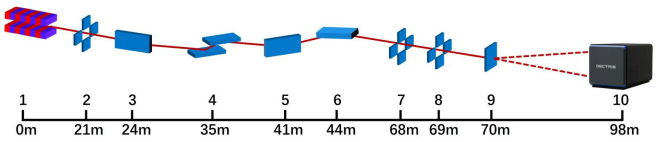

Fig. 1. (Color online) Schematic of the experimental setup: 1. Undulator; 2. Four-blade slits 1; 3. Horizontal deflection mirror; 4. Double multilayer monochromator; 5. Horizontal focusing mirror; 6. Vertical focusing mirror; 7. Four-blade slits 2; 8. Four-blade slits 3; 9. Sample; 10. Detector. [49]

The experiment was conducted at the BL10U1 USAXS beamline of SSRF, and the schematic diagram of the experimental setup is shown in Fig. 1. The incident beam emitted from the undulator was monochromated by a double multilayer monochromator after passing through the four-blade slits 1. The photon energy and energy resolution ($\Delta E/E$) were $10\,\mathrm{keV}$ ($\lambda = 0.124\,\mathrm{nm}$) and 5.8×10^{-3}, respectively. The beam was subsequently focused using horizontal and vertical focusing mirrors with the focal point at the detector. The partially coherent light required for the experiment was selected using upstream four-blade slits 2 and 3. A pinhole with a diameter of $100\,\mu\mathrm{m}$ was placed upstream of the sample to reduce the beam size and increase the coherence of the incident beam on the sample. The scattering signal of the sample was recorded using an area detector (EIGER X 4M) located $27.6\,\mathrm{m}$ downstream from the sample. The effective pixel number of the detector was 2070×2167 with a pixel size of $75\,\mu\mathrm{m} \times 75\,\mu\mathrm{m}$. Its frame rate could reach $750\,\mathrm{Hz}$, i.e. $1.34\,\mathrm{ms}$ minimum exposure period. In this experiment, the available q-range (scattering wave vector range) was approximately $1.2\times10^{-2}\ \mathrm{nm}^{-1}$–$2.0\times10^{-1}\ \mathrm{nm}^{-1}$. The scattering wave vector q was determined from the scattering angle 2θ using the formula $q = 4\pi\sin(\theta)/\lambda$. To ensure the repeatability of the experiment and accuracy of the results, the experiments were repeated three times under the same conditions, with each run collecting 1000 speckle patterns. Six exposure periods (2, 5, 10, 20, 50, and $100\,\mathrm{ms}$) were used to evaluate the temporal resolving ability of the XPCS study.

IV. DLS

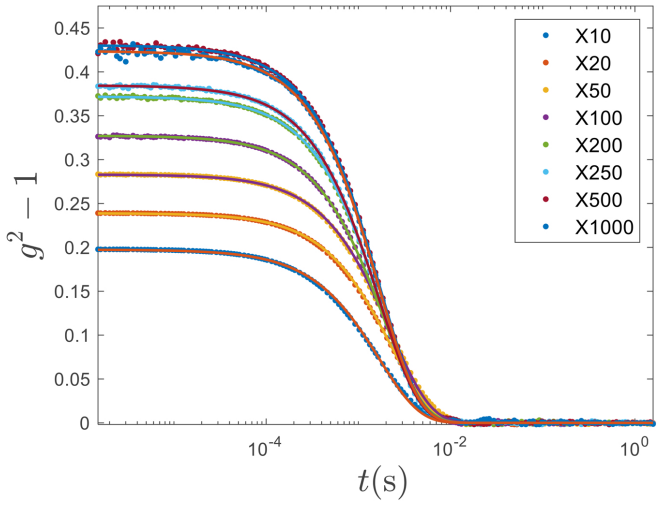

Fig. 2. (Color online) Correlation data (points) obtained using DLS measurements of the stock solution at different dilution factors or concentrations ($X10 \sim 0.1$ %, $X20 \sim 0.05$ %, $X50 \sim 0.02$ %, $X100 \sim 0.01$ %, $X200 \sim 0.005$ %, $X250 \sim 0.004$ %, $X500 \sim 0.002$ %, $X1000 \sim 0.001$ %.). These solid lines are the fitting curves for the correlation data.

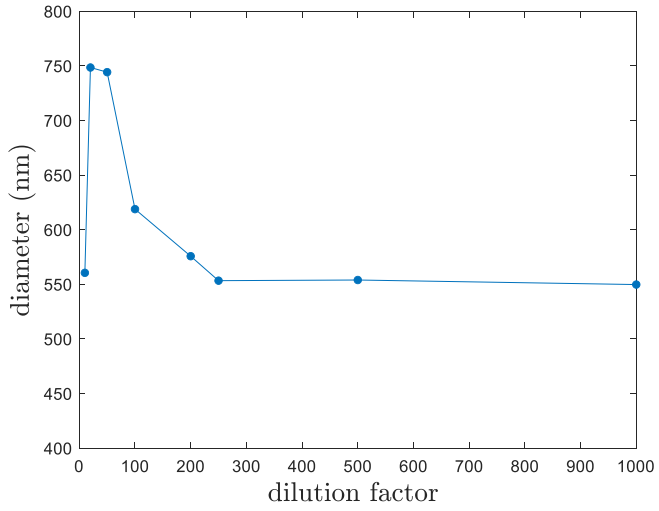

Fig. 3. Hydrodynamic diameters of silica in water suspensions of different concentrations obtained using the fitting results. The x axis represents the dilution factor of the stock solution.

Prior to the XPCS experiment, the silica suspension was pre-characterized using DLS technology. The coherent light source was a laser with a wavelength of $\lambda_{\text{laser}} = 633\,\text{nm}$, and the size of the laser beam was adjusted to 2 mm using a diaphragm. The laser was then directed into the sample contained in the cuvette, causing the light to scatter and form a speckle pattern. The scattered signal was collected by a detector (photomultiplier tube, PMT) after passing through an order-sorting aperture (OSA) with a diameter of $70\,\mu\text{m}$. The PMT was located at a scattering angle of $\pi/2$ (90°). The signal was displayed on a computer after correlation using a correlator (ALV-7004/USB-FAST). The entire experimental setup was placed in a dark room to avoid the influence of natural light. Additionally, considering the high sensitivity of the PMT to light, an extra layer of darkroom was added around the detector to prevent stray signals from the laser and allow only the OSA to receive light. The acquisition time for each signal was set to 10 s, and the process was repeated ten times to obtain the average value.

The stock solution was diluted with water to different concentrations, and then these samples were placed in the cuvette for DLS measurement (Fig. 2). The experimental temperature was maintained at 297 K. The measured results were fitted (Fig. 2, solid line) using the equation $g^2-1 = \beta e^{-2\frac{t}{\tau}}$ to obtain the relaxation time τ, where β represents the speckle contrast. According to the experimental parameters, the hydrodynamic diameters of silica (Fig. 3) can be obtained from the relaxation times τ of the samples. Figure 3 shows that in the case of a low dilution factor, the hydrodynamic diameter of silica first increases and then decreases owing to the influence of multiple scattering. The influence of multiple scattering becomes negligible with increasing dilution factor. The hydrodynamic diameter of silica is stable at approximately $550\,\text{nm}$, which is slightly larger than that obtained by SEM. This is consistent with the expected results [23].

These findings indicate that DLS is indeed constrained by the sample concentration and that multiple scattering significantly affects the experimental results. Therefore, determining the dynamic behavior of silica in the stock solution using the traditional DLS method is impossible because of the influence of multiple scattering. However, XPCS can easily overcome the influence of multiple scattering using hard X-rays.

V. SMALL ANGLE X-RAY SCATTERING (SAXS)

The two-dimensional (2D) small angle X-ray scattering (SAXS) data presented in Fig. 4 was generated by overlaying 1000 frames of speckle patterns collected for each of the three sets of data. The results from the three sets of data were averaged. The exposure period was $50\,\text{ms}$, corresponding to a total exposure time of $50\ s$ per frame. The 2D SAXS pattern was azimuthally integrated to obtain the one-dimensional (1D) SAXS profile (Fig. 5 point), illustrating the scattering intensity $I(q)$ with respect to the scattering wave vector q. The signals of bad pixels, gaps, and beamstop were excluded from data processing. By fitting the 1D SAXS data (Fig. 5 line), the diameter of the silica particles was determined to be $R_{\text{SAXS}} = 528.2\,\text{nm}$ (In the high q range, the difference between the SAXS results and fitted curve is primarily because of the weak scattered signal at high q, which is considerably affected by noise.). This size was consistent with that obtained by SEM, indicating that the size of the silica particles produced via rotary evaporation did not change significantly, and substantial agglomeration was not observed. The agreement between the SAXS, SEM, and DLS measurements

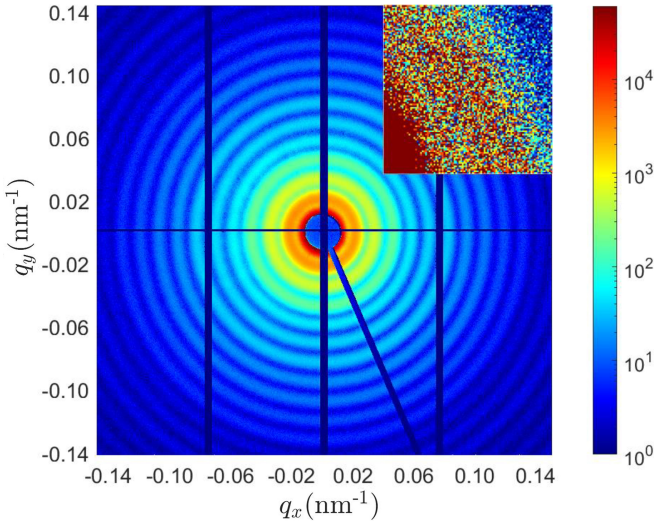

Fig. 4. (Color online) Two-dimensional (2D) SAXS from the sample overlaying 1000 frames collected continuously within 50 s. The result was further averaged from three repeated measurements to improve the statistics. The x and y axes are represented by the scattering vectors q_x and q_y, respectively. For a clear view, the logarithm of the scattering signal intensity is taken to the base 10. The illustration in the upper right corner is a speckle image.

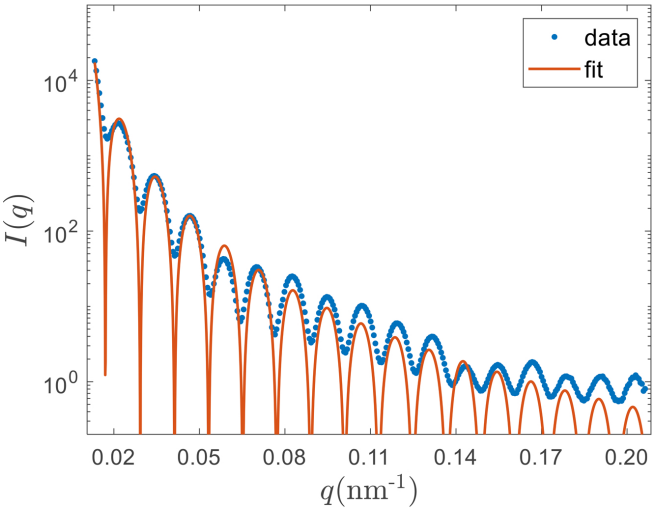

Fig. 5. (Color online) One-dimensional (1D) SAXS data derived by using the azimuthal averaging of scattering signals from the sample shown in Fig. 4. Point: SAXS scattering intensity $I(q)$ with respect to scattering wave vector q; Line: fitting of silica size (considering the silica as homogeneous spherical particles) [50]. For a clear view, the logarithm of the scattering signal intensity is taken to the base 10.

proves the reliability of the size and structure of the silica particles in the stock solutions. Therefore, a comprehensive understanding of the particle size and potential aggregation phenomena was obtained by employing the SAXS and DLS techniques.

VI. X-RAY PHOTON CORRELATION SPECTROSCOPY (XPCS)

A. Theory

To investigate the dynamic properties of silica, the obtained scattering patterns were correlated using the intensity correlation equation. The influence of photon flux variation on the results was minimized by applying the two-time correlation (TTC) method to analyze the sample dynamics [51]:

$$g^2(q,t_1,t_2) = \frac{\langle I(q,t_1)I(q,t_2)\rangle}{\langle I(q,t_1)\rangle \langle I(q,t_2)\rangle} \tag{2}$$

where $I(q,t_{1,2})$ is the intensity value at q and $t_{1,2}$; $\langle\cdots\rangle$ represents the average of all pixels; and $|t_1 - t_2| = \tau$ indicates the delay time. When the sample is in equilibrium during the observation time, the TTC can be expressed as [25, 52]:

$$g^2(q,\tau) = \langle g^2(q,t_1,t_2)\rangle \tag{3}$$

Averaging the corresponding data with the same delay time τ improves the SNR of the results. The intensity correlation function $g^2(q,\tau)$ can be related to the first-order correlation function $g^1(q,\tau)$ through the Siegert relation [1]:

$$g^2(q,\tau) = 1 + \beta\left|(g^1(q,\tau))\right|^2 \tag{4}$$

Here, β represents the speckle contrast, which depends on the coherence of the incident beam, optical layout of the beamline and pixel size of the detector. In this study, the diluted colloidal suspension was expected to exhibit Brownian motion [27, 52, 53], such that

$$g^1(q,\tau) = e^{-(\Gamma(q)t)} \tag{5}$$

Combining Eqs. 4 and 5, the correlation equation can be simplified to:

$$g^2(q,\tau) = 1 + \beta e^{-2(\Gamma(q)t)} \tag{6}$$

$\Gamma(q) = 1/\tau_c(q)$ represents the relaxation rate, which is the reciprocal of the characteristic relaxation time $\tau_c(q)$:

$$\tau_c(q) = \frac{1}{Dq^2} \tag{7}$$

D represents the Stokes-Einstein diffusion constant, which can be expressed as

$$D = \frac{k_B T}{6\pi\eta R_H}, \tag{8}$$

where k_B, T, η , and R_H represent the Boltzmann constant, thermodynamic temperature, viscosity coefficient of the solvent, and hydrodynamic radius of the silica particles, respectively.

B. Results and discussion

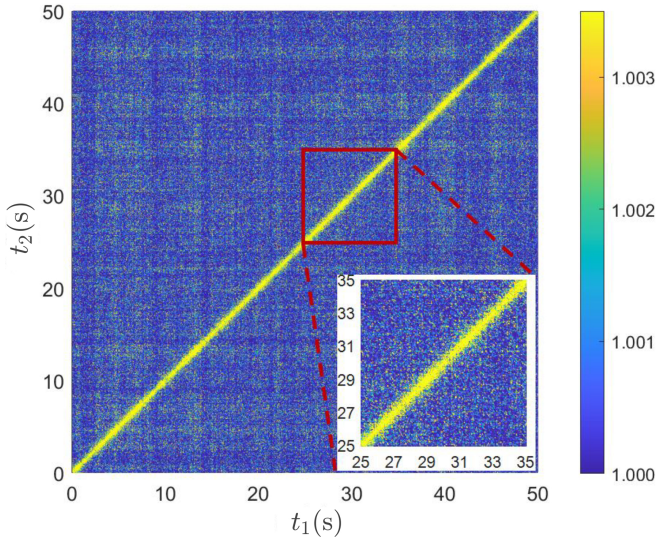

Fig. 6. (Color online) TTC derived from the correlation calculation of 1000 frames of speckle patterns using Eq. 2. $t_{1,2}$ indicates the time of the experiment, where the exposure period is 50 ms, $q = 2.13 \times 10^{-2}$ nm^{-1} ($\Delta q = 2.06 \times 10^{-3}$ nm^{-1}). The inset figure shows a partially enlarged view of the results of the experimental time $25 - 35$ s.

The two time correlation (TTC) maps in Fig. 6 exhibit no significant change (narrowing) at the midridge line on the diagonal in the image during the entire experiment. This indicates that the silica in the sample is in equilibrium dynamics. Therefore, the effects of sample heating and damage by X-rays on the sample were negligible for the XPCS experiments conducted in this work.

The data collected from the same sample at different exposure periods were correlated and fitted using Eq. 6 (Fig. 7). First, all the data were fitted well using a single exponential model. Second, data with shorter exposure periods exhibited lower SNR. From Eq. 1, it is natural to obtain lower SNR when lower exposure periods reduced the intensity I_{pix} with all other parameters kept constant. Nonetheless, the SNR of the lowest exposure period (2 ms) was sufficient for the correlation analysis. The SNR of the low-exposure periods could be significantly increased by increasing $N_{\rm fr}$ or $N_{\rm rep}$. Third, and most importantly, despite the significantly different exposure periods, all correlation curves exhibited similar decay behaviors. This is further demonstrated by the relaxation rate analysis below.

The relaxation rate Γ of the sample obtained from fitting is shown in Fig. 8 and the relaxation rates obtained at different exposure periods are consistent. The dashed line is the guide line for the eye, and the error bars are the standard deviations of the three repetitions. The Γ values for different exposure periods are almost unchanged, indicating the feasibility of XPCS experiments with millisecond exposures in SSRF [48, 54–57]. In addition, Fig. 8 shows that the standard deviation decreases with increasing exposure time. From Eq. 1, this can be attributed to an increase in $I_{\rm pix}$, which improves the SNR of the result. Therefore, we can improve the SNR by increasing the number of frames ($N_{\rm fr}$) collected, thereby reducing the standard deviation of the millisecond exposure results. In summary, the standard deviation of our millisecond-exposure results is usable and can be reduced to ensure realistic dynamic sampling.

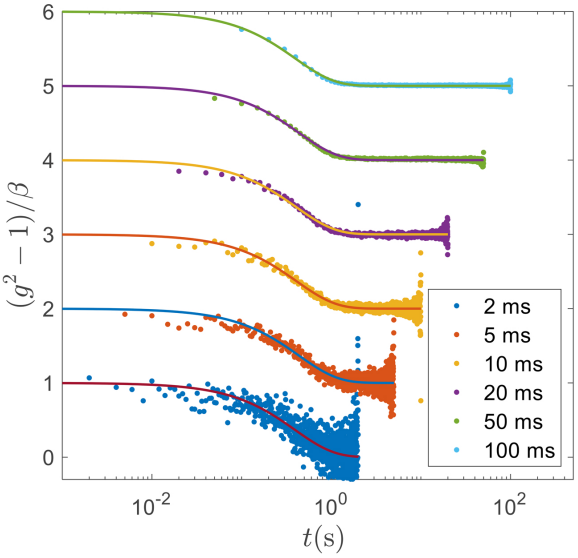

Fig. 7. (Color online) Correlation function of the sample at different exposure periods, where $q = 2.13 \times 10^{-2}$ nm^{-1} ($\Delta q = 2.07 \times 10^{-3}$ nm^{-1}), and $g^2(q,\tau)$ is normalized. For clarity, $g^2(q,\tau)$ was shifted vertically. Points and lines refer to correlation data and fitted curves using Eq. 6, respectively. These results were averaged over three replicated measurements to improve the statistics.

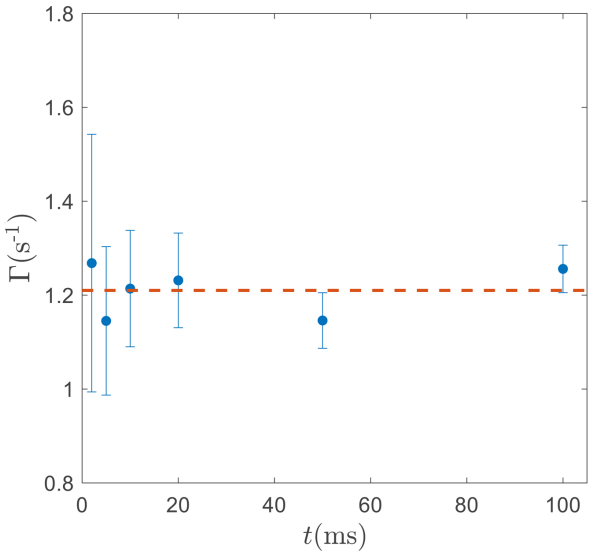

Fig. 8. Relaxation rate Γ obtained by fitting the correlation function at different exposure periods (Fig. 7), and the abscissa represents the different exposure periods (2, 5, 10, 20, 50, and 100 ms). The dashed line is the guide line for the eye. These results were averaged over three replicated measurements to improve the statistics.

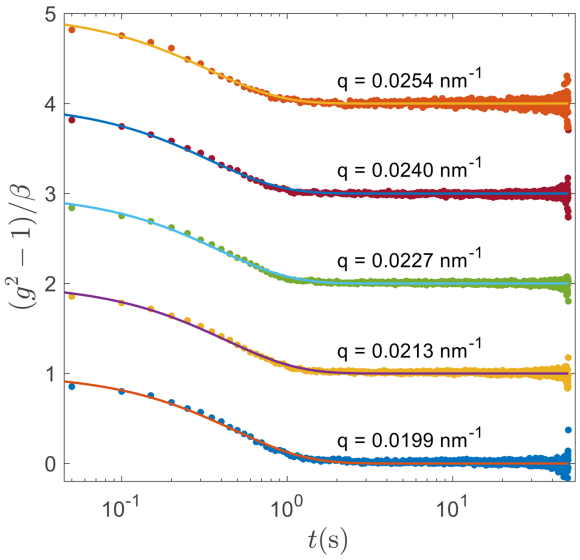

Fig. 9. (Color online) Correlation functions under different scattering wave vector q values ($\Delta q = 6.88 \times 10^{-4}$ nm^{-1}), where the exposure period is 50 ms, and $g^2(q,\tau)$ is normalized. For clarity, $g^2(q,\tau)$ was shifted vertically. Points and lines refer to correlation data and fitted curves using Eq. 6 at different q values, respectively. These results were averaged over three replicated measurements to improve the statistics.

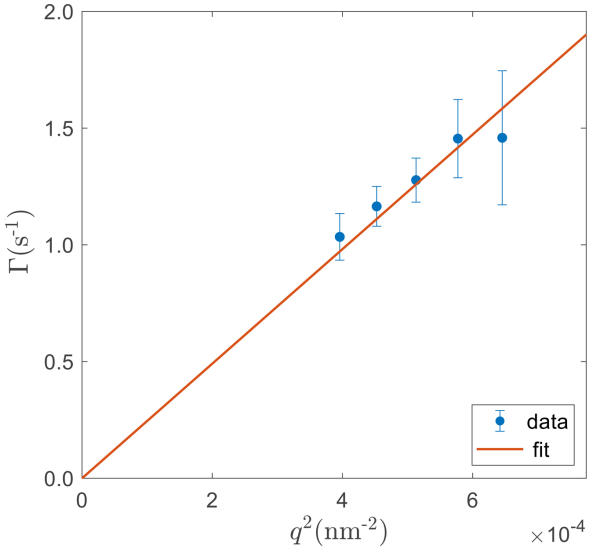

Fig. 10. Relationship between the relaxation rate Γ and q^2. The points refer to the relaxation rate Γ under different q^2 values obtained from the fitting of Fig. 9. The line refers to the linear fitting of the points, which has been forced through the origin. These results were averaged over three replicated measurements to improve the statistics.

The relationship between $g^2(q,\tau)$ and different q values in the data was correlated and fitted using Eq. 6 (Fig. 9). The decay is slower at lower q values because the characteristic decay time decreases with q. Fig. 10 shows that the relaxation rate (points) of the sample varies linearly with q^2. The Stokes-Einstein diffusion constant $D = 2425$ nm^2/s is obtained by linear fitting with $\Gamma = D \times q^2$. This proves that the silica in the sample undergoes Brownian motion.

Because of the incomplete water removal by the rotary evaporator and the hygroscopicity of glycerol, the sample inevitably contains water. The water content of glycerol strongly affects the viscosity [58] and thus, the viscosity of the sample cannot be accurately determined. However, for a silica sphere, R_{H} is slightly larger than R_{SAXS} [23]. We assumed that $R_{\mathrm{H}} = R_{\mathrm{SAXS}}$ [48] and then estimated the viscosity of the sample using Eq. 8, which yielded $\eta = 0.34$ Pa · s. Based on the empirical formula [59],

$$\eta = \eta_{\mathrm{w}}^{\alpha}\eta_{\mathrm{g}}^{1-\alpha} \tag{9}$$

where $\eta_{\mathrm{w}}^{\alpha}$ and $\eta_{\mathrm{g}}^{1-\alpha}$ are the viscosities of water and glycerol, respectively, α can be expressed as a function of the glycerol mass concentration C_{m}:

$$\alpha = 1 - C_{\mathrm{m}} + \frac{abC_{\mathrm{m}}(1-C_{\mathrm{m}})}{aC_{\mathrm{m}} + b(1-C_{\mathrm{m}})} \tag{10}$$

a and b are the coefficients of the temperature T_{c} in Celsius, where $a = 0.705 - 0.0017\,T_{\mathrm{c}}$ and $b = (4.9 + 0.036\,T_{\mathrm{c}})\,a^{2.5}$. The water mass concentration in the sample was estimated to be approximately 5.2 %. This portion of water, which is difficult to remove, makes it challenging to determine the viscosity of the sample. Consequently, it is difficult to calculate the hydrodynamic diameter of silica using the Stokes-Einstein diffusion constant D and compare it with the results obtained from SEM or SAXS. Using another solvent that absorbs less water can help solve this problem. Nonetheless, we successfully demonstrated a systematic XPCS study of a highly concentrated silica suspension at SSRF.

VII. SUMMARY

XPCS is an emerging technique with great potential for characterizing sample dynamics at molecular and atomic scales. Its advantages over DLS include high penetration capability, high spatial resolution, and reduced multi-scattering. However, the requirement for coherent X-ray sources limits its accessibility, as third-generation synchrotrons such as SSRF, cannot easily provide sufficient coherence. After the recent upgrade of SSRF, the newly commissioned BL10U1 USAXS beamline provides an ideal platform for XPCS experiments because of its unique properties such as relatively high coherence, high brilliance, and long sample-to-detector distance.

In this study, we successfully performed XPCS studies on a silica suspension model system. The linear $\Gamma - q^2$ dependence demonstrates that the correct Brownian motion dynamics was obtained. Careful collimation of micrometer optics ensured low parasitic scattering and high coherence, and a newly established framework for data analysis enabled the effective extraction of dynamic information from scattering

images. Consequently, we achieved a millisecond time resolution, which is at the same level as most XPCS experiments at modern synchrotrons.

The establishment of the XPCS platform is expected to provide new options for researchers in China and abroad, and facilitate the study of various nanoscale and microscale samples such as colloidal suspensions, polymers, glass, biomacromolecules, and strongly related materials. This powerful tool will enable researchers gain valuable insights into the dynamic properties of these systems in their natural environment and contribute to a deeper understanding of their behavior and properties.

ACKNOWLEDGMENTS

The authors thank the staff of USAXS beamline (BL10U1) at SSRF for their support during the beamtime. The authors thank the user experimental assistance system of SSRF for their assistance.

AUTHOR CONTRIBUTIONS

Huai-Dong Jiang, and Ren-Zhong Tai contributed to the overall research concept and supervision of this study. Yi-Hui Xu, Chen-Hui Cui, Zi-Mu Zhou, Lin-Feng Wei, and Song-Lin Li participated in material preparation, data collection, data processing program writing, and data analysis. Feng Tian, Xiu-Hong Li provided experimental suggestions and optimized experimental conditions. Zhi Guo and Yi-Hui Xu provided fund support, reviewed the manuscript. The first draft of the manuscript was written by Chen-Hui Cui and all authors commented on previous versions of the manuscript. All authors read and approved the final manuscript.

CONFLICT OF INTEREST

Ren-Zhong Tai is an editorial board member for Nuclear Science and Techniques and was not involved in the editorial review, or the decision to publish this article. All authors declare that there are no competing interests.

[1] B.J. Berne, R. Pecora, *Dynamic light scattering: With applications to chemistry, biology, and physics*. (John Wiley & Sons, 2000).

[2] R. Yan, Z. Guo, R.Z. Tai *et al*., Observation of long range correlation dynamics in $BaTiO_3$ near TC by photon correlation spectroscopy. Appl. Phys. Rev. **93**, 192908 (2008). doi: 10.1063/1.3025465

[3] C.L. Song, R. Yan, Z. Guo *et al*., Temperature dependence of relaxation time for polarization clusters in $BaTiO_3$ near TC. Nuclear Techniques **33(4)**, 258–261 (2010). (in Chinese)

[4] R. Yan, Z. Guo, R.Z. Tai, Observation of relaxation time for polarization clusters in BaTiO3 near TC by photon correlation spectroscopy. Nuclear Techniques **32(6)**, 439–442 (2009). (in Chinese)

[5] M.J. Zhang, Z. Guo, R.Z. Tai *et al*., Observation of dual relaxation dynamics of polarization clusters in barium titanate by photon correlation spectroscopy. Jpn. J. Appl. Phys. **54(4)**, 042401 (2015). doi: 10.7567/JJAP.54.042401

[6] P.N. Segrè, O.P. Behrend, P.N. Pusey, Short-time Brownian motion in colloidal suspensions: Experiment and simulation. Phys. Rev. E. **52(5)**, 5070 (1995). doi: 10.1103/PhysRevE.52.5070

[7] G. Grübel, F. Zontone, Correlation spectroscopy with coherent X-rays. J. Alloy. Compd. **362(1-2)**, 3-11 (2004). doi: 10.1016/S0925-8388(03)00555-3

[8] D. Lumma, L.B. Lurio, S.G.J. Mochrie, Area detector based photon correlation in the regime of short data batches: Data reduction for dynamic x-ray scattering. Rev. Sci. Instrum. **71(9)**, 3274–3289 (2000). doi: 10.1063/1.1287637

[9] O.G. Shpyrko, X-ray photon correlation spectroscopy. J. Synchrotron. Radiat. **21(5)**, 1057–1064 (2014). doi: 10.1107/S1600577514018232

[10] J.R. Massey, R.C. Temple, T.P. Almeida *et al*., Asymmetric magnetic relaxation behavior of domains and domain walls observed through the FeRh first-order metamagnetic phase transition. Phys. Rev. B **102(14)**, 144304 (2020). doi: 10.1103/PhysRevB.102.144304

[11] C.G. Schroer, I. Agapov, W. Brefeld *et al*., PETRA IV: the ultralow-emittance source project at DESY. J. Synchrotron. Radiat. **25(5)**, 1277–1290 (2018). doi: 10.1107/S1600577518008858

[12] J.B. Svensson, T.K. Charles, O. Lundh *et al*., Third-order double-achromat bunch compressors for broadband beams. Phys. Rev. Accle. Beams. **22(10)**, 104401 (2019). doi: 10.1103/PhysRevAccelBeams.22.104401

[13] D. Chenevier, A. Joly, ESRF: inside the extremely brilliant source upgrade. Synchrotron Radiation News. **31(1)**, 32–35 (2018). doi: 10.1080/08940886.2018.1409562

[14] J. Dooling, M. Borland, W. Berg *et al*., Collimator irradiation studies in the Argonne Advanced Photon Source at energy densities expected in next-generation storage ring light sources. Phys. Rev. Accel. Beams. **25(4)**, 043001 (2022). doi: 10.1103/PhysRevAccelBeams.25.043001

[15] Y. Jiao, G. Xu, X.H. Cui *et al*., The HEPS project. J. Synchrotron Radiat. **25(6)**, 1611–1618 (2018). doi: 10.1107/S1600577518012110

[16] Z.H. Bai, G.W. Liu, T.L.He *et al*., Preliminary physics design of the Hefei Advanced Light Facility storage ring. High Power Laser and Particle Beams. **34**, 104003 (2022). doi: 10.11884/HPLPB202234.220137

[17] T. Tschentscher, C. Bressler, J. Grünert *et al*., Photon beam transport and scientific instruments at the European XFEL. Appl. Sci. **7(6)**, 592 (2017). doi: 10.3390/app7060592

[18] A. Halavanau, F.J. Decker, C. Emma *et al*., Very high brightness and power LCLS-II hard X-ray pulses. J. Synchrotron. Radiat. **26(3)**, 635–646 (2019). doi: 10.1107/S1600577519002492

[19] C.J. Milne, T. Schietinger, M. Aiba *et al*., SwissFEL: the Swiss X-ray free electron laser. Appl. Sci. **7(7)**, 720 (2017). doi: 10.3390/app7070720

[20] M. Yabashi, H. Tanaka, K. Tono *et al*., Status of the SACLA Facility. Appl. Sci. **7(6)**, 604 (2017). doi: 10.3390/app7060604

[21] Z.T. Zhao, D. Wang, Q. Gu *et al*., Status of the SXFEL Facility. Appl. Sci. **7(6)**, 607 (2017). doi: 10.3390/app7060607

[22] Y.X. Zhang, J.F. Chen, D. Wang . RF design optimization for the SHINE 3.9 GHz cavity. Nucl. Sci. Tech. **31(7)**, 73 (2020). doi: 10.1007/s41365-020-00772-z

[23] J. Möller, Y. Chushkin, S. Prevost *et al*., Multi-speckle X-ray photon correlation spectroscopy in the ultra-small-angle X-ray scattering range. J. Synchrotron Radiat. **23(4)**, 929-936 (2016). doi: 10.1107/S1600577516008092

[24] K. Switalski, J. Fan, L. Li *et al*., Direct measurement of Stokes–Einstein diffusion of Cowpea mosaic virus with 19 μs-resolved XPCS. J. Synchrotron. Radiat. **29**, 1429–1435 (2022). doi: 10.1107/S1600577522008402

[25] S.K. Sinha, Z. Jiang, L.B. Lurio *et al*., X-ray photon correlation spectroscopy studies of surfaces and thin films. Adv. Mater. **26(46)**, 7764–7785 (2014). doi: 10.1002/adma.201401094

[26] G. Grübel, F. Zontone, Correlation spectroscopy with coherent X-rays. J. Alloy. Compd. **362(1-2)**, 3–11 (2004). doi: 10.1016/S0925-8388(03)00555-3

[27] S.B. Dierker, R. Pindak, R.M. Fleming *et al*., X-ray photon correlation spectroscopy study of Brownian motion of gold colloids in glycerol. Phys. Rev. Lett. **75(3)**, 449 (1995). doi: 10.1103/PhysRevLett.75.449

[28] T. Hoshino, D. Murakami, Y. Tanaka *et al*., Dynamical crossover between hyperdiffusion and subdiffusion of polymer-grafted nanoparticles in a polymer matrix. Phys. Rev. E. **88(3)**, 032602 (2013). doi: 10.1103/PhysRevE.88.032602

[29] J. Carnis, W. Cha, J. Wingert *et al*., Demonstration of feasibility of x-ray free electron laser studies of dynamics of nanoparticles in entangled polymer melts. Sci. Rep-UK. **4(1)**, 6017 (2014). doi: 10.1038/srep06017

[30] Z. Evenson, B. Ruta, S. Hechler *et al*., X-ray photon correlation spectroscopy reveals intermittent aging dynamics in a metallic glass. Phys. Rev. Lett. **115(17)**, 175701 (2015). doi: 10.1103/PhysRevLett.115.175701

[31] B. Ruta, Y. Chushkin, G. Monaco *et al*., Atomic-scale relaxation dynamics and aging in a metallic glass probed by x-ray photon correlation spectroscopy. Phys. Rev. Lett. **109(16)**, 165701 (2012). doi: 10.1103/PhysRevLett.109.165701

[32] M. Reiser, A. Girelli, A. Ragulskaya *et al*., Resolving molecular diffusion and aggregation of antibody proteins with megahertz X-ray free-electron laser pulses. Nat. Commun. **13(1)**, 5528 (2022). doi: 10.1038/s41467-022-33154-7

[33] L.B. Lurio, G.M. Thurston, Q. Zhang *et al*., Use of continuous sample translation to reduce radiation damage for XPCS studies of protein diffusion. J. Synchrotron. Radiat. **28(2)**, 490–498 (2021). doi: 10.1107/S1600577521000035

[34] J. Möller, M. Sprung, A. Madsen *et al*., X-ray photon correlation spectroscopy of protein dynamics at nearly diffraction-limited storage rings. IUCrJ. **6(5)**, 794–803 (2019). doi: 10.1107/S2052252519008273

[35] R.Z. Tai, K. Namikawa, M. Kishimoto *et al*., Picosecond Snapshot of the Speckles from Ferroelectric BaTiO3 by Means of X-Ray Lasers. Phys. Rev. Lett. **89(25)**, 257602 (2002). doi: 10.1103/PhysRevLett.89.257602

[36] K. Namikawa, M. Kishimoto, K. Nasu *et al*., Direct observation of the critical relaxation of polarization clusters in $BaTiO_3$ using a pulsed X-ray laser technique. Phys. Rev. Lett. **103(19)**, 197401 (2009). doi: 10.1103/PhysRevLett.103.197401

[37] Z.J. Qiu, K. Li, H.L. Xie *et al*., Study of 20 Hz high spatial-temporal resolution monochromatic X-ray dynamic micro-CT. Nuclear Techniques **46(7)**, 070101 (2023). doi: 10.11889/j.0253-3219.2023.hjs.46.070101

[38] H.T. Li, B. Zhao, X.Z. Zhang *et al*., Development of a portable laser heating device for synchrotron radiation in situ experiment. NUCLEAR TECHNIQUES. **46(2)**, 020101 (2023). doi: 10.11889/j.0253-3219.2023.hjs.46.020101

[39] H.Z. Liu, L. Ji, S.Q. Gu *et al*., Upgrade of transmission XAFS data acquisition system upgrade of Shanghai Synchrotron Radiation Facility BL14W1 beamline station. Nuclear Techniques **45(7)**, 070103 (2022). doi: 10.11889/j.0253-3219.2022.hjs.45.070103

[40] S.S. Qu, Z. Guo, R.Z. Tai *et al*., Design of soft X-ray photon correlation spectroscopy device. Nuclear Science **42(4)**, 040103 (2019). doi: 10.11889/j.0253-3219.2019.hjs.42.040103

[41] X. Yang, J.F. Cao, J.Q. Li *et al*., Picosecond time-resolved X-ray ferromagnetic resonance measurements at Shanghai Synchrotron Radiation Facility. Nucl. Sci. Tech. **33(5)**, 63 (2022). doi: 10.1007/s41365-022-01037-7

[42] Z.J. Xu, C.P. Wang, H.G. Liu *et al*., Low-dose, high-resolution and high-efficiency ptychography at STXM beamline of SSRF. J. Phys. Conf. Ser. **849(1)**, 012033 (2017). doi: 10.1088/1742-6596/849/1/012033

[43] C.P. Wang, Z.J. Xu, H.G. Liu *et al*., Soft X-ray ptychography method at SSRF. Nucl. Sci. Tech. **28(6)**, 74 (2017). doi: 10.1007/s41365-017-0227-6

[44] G.Z. Zhou, Z. Hu, S.M. Yang *et al*., Preliminary exploration of hard X-ray coherent diffraction imaging method at SSRF. Acta. Phys. Sin. **69(3)**, 034102 (2020). doi: 10.7498/aps.69.20191586

[45] C. Caronna, Y. Chushkin, A. Madsen *et al*., Dynamics of nanoparticles in a supercooled liquid. Phys. Rev. Lett. **100(5)**, 055702 (2008). doi: 10.1103/PhysRevLett.100.055702

[46] H. Conrad, F. Lehmkuehler, B. Fischer *et al*., Correlated heterogeneous dynamics in glass-forming polymers. Phys. Rev. E. **91(4)**, 042309 (2015). doi: 10.1103/PhysRevE.91.042309

[47] E.B. Trigg, L. Wiegart, A. Fluerasu *et al*., Dynamics of polymerization and gelation in epoxy nanocomposites via X-ray photon correlation spectroscopy. Macromolecules **54(13)**, 6575–6584 (2021). doi: 10.1021/acs.macromol.1c00727

[48] F. Lehmkühler, P. Kwaśniewski, W. Roseker *et al*., Sequential single shot x-ray photon correlation spectroscopy at the SACLA free electron laser. Sci. Rep-UK. **5(1)**, 17193 (2015). doi: 10.1038/srep17193

[49] Z. Hu, C.X. Hong, W.Q. Hua *et al*., Online monitoring of hard X-ray beam at SSRF. Acta Optica Sinica. **41(15)**, 1534001 (2021). doi: 10.3788/AOS202141.1534001

[50] J. Als-Nielsen, D. *McMorrow, Elements of modern X-ray physics*. (John Wiley & Sons, Ltd, 2011), pp. 113-146

[51] M. Sutton, K. Laaziri, F. Livet *et al*., Using coherence to measure two-time correlation functions. Opt. Express. **11(19)**, 2268–2277 (2003). doi: 10.1364/OE.11.002268

[52] F. Lehmkühler, W. Roseker, G. Grübel, From femtoseconds to hours—measuring dynamics over 18 orders of magnitude with coherent x-rays. Appl. Sci. **11(13)**, 6179 (2021). doi: 10.3390/app11136179

[53] Y. Xu, M. Sikorski, J.D. Fan *et al*., Thermal effects of beam profiles on X-ray photon correlation spectroscopy at megahertz X-ray free-electron lasers. Opt. Express. **30(23)**, 42639–42648 (2022). doi: 10.1364/OE.464852

[54] W. Jo, R. Rysov, F. Westermeier *et al*., Demonstration of 3D photon correlation spectroscopy in the hard X-ray regime. Opt. Lett. **47(2)**, 293–296 (2022). doi: 10.1364/OL.444190

[55] G.X. Ju, D.W. Xu, M.J. Highland *et al*., Coherent X-ray spectroscopy reveals the persistence of island arrangements during

layer-by-layer growth. Nat. Phys. **15(6)**, 589–594 (2019). doi: 10.1038/s41567-019-0448-1

[56] F. Dallari, A. Jain, M. Sikorski *et al*., Microsecond hydrodynamic interactions in dense colloidal dispersions probed at the European XFEL. IUCrJ. **8(5)**, 775–783 (2021). doi: 10.1107/S2052252521006333

[57] M. Reiser, J. Hallmann, J. Moller *et al*., Photo-Controlled Dynamics and Transport in Entangled Wormlike Micellar Nanocomposites Studied by XPCS. Macromolecules. **55(19)**, 8757–8765 (2022). doi: 10.1021/acs.macromol.2c01326

[58] J.B. Segur, H.E. Oberstar, Viscosity of glycerol and its aqueous solutions. Ind. Eng. Chem. **43(9)**, 2117–2120 (1951). doi: 10.1021/ie50501a040

[59] N.S. Cheng, Formula for the viscosity of a glycerol-water mixture. Ind. Eng. Chem. Res. **47(9)**, 3285-3288 (2008). doi: 10.1021/ie071349z